Zhu *et al.*
Chinese Journal of Mechanical Engineering (2023) 36:20
https://doi.org/10.1186/s10033-023-00844-2

Chinese Journal of Mechanical Engineering

ORIGINAL ARTICLE

Open Access

Parameters Calibration of the GISSMO Failure Model for SUS301L-MT

Tao Zhu[1*], Haoxu Ding[1], Chao Wang[1], Yuxin Liu[2], Shoune Xiao[1], Guangwu Yang[1] and Bing Yang[1]

Abstract

With the development of the rail transit industry, more attention has been paid to the passive safety of rail vehicles. Structural damage is one of the main failure behaviors in a rail vehicle collision, but it has been paid little attention to in past research. In this paper, the quasi-static fracture experiments of SUS301L-MT under different stress states were carried out. The mechanical fracture properties of this material were studied, and the corresponding finite element simulation accuracy was improved to guide the design of vehicle crashworthiness. Through the tests, the fracture behavior of materials with wide stress triaxiality was obtained, and each specimen's fracture locations and fracture strains were determined. Parameters of a generalized incremental stress state dependent damage model (GISSMO) of the material were calibrated, and the model's accuracy was verified with test results from a 45° shear specimen. The GISSMO failure model accurately reflected the fracture characteristics of the material. The mesh dependency of this model was modified and discussed. The results show that the simulation agrees well with experimental data for the force-displacement curve after correction, but the strain distribution needs to be further studied and improved.

Keywords SUS301L-MT, Fracture failure, GISSMO model, Finite element simulation, Stress state

1 Introduction

Ductile fracture of metal components is a critical failure mode of industrial machinery products [1]. The study of ductile fracture of metal is usually divided into crack generation and propagation [2, 3] and its application in structure [4]. For the former, the classic strength theory, represented by the Von Mises strength criterion [5], applies the fracture behavior of material standard specimens to the local fracture of structural members roughly. With this method, the difference between the material and the component under load is ignored to some extent. It has specific applicability to the component's initial yielding or initial cracking, but the prediction of the entire ductile fracture process needs to be more accurate.

*Correspondence:
Tao Zhu
zhutao034@swjtu.cn
[1] State Key Laboratory of Traction Power, Southwest Jiaotong University, Chengdu 610031, China
[2] FAW Jiefang Automobile Co., LTD, Changchun 130011, China

McClintock [6] found that the growth and connection of microscopic voids cause ductile damage. Furthermore, the stress state is an essential factor affecting ductile damage. Based on this view, Gurson [7], Rice and Tracey [8], and Tvergaard and Needleman et al. [9–12] eventually developed the GTN model. In this model, material fracture occurs when the volume of the fraction of the holes increases to a certain threshold [13]. However, the complexity of the damage potential function and the quantitative description of microscopic damage make it more challenging to apply to the fracture process of engineering components [14, 15].

In contrast, the yield / fracture criterion models are widely used in engineering because of their simplicity and convenience. There are currently three main models: the J-C model, the B-W model, and the MMC model. The J-C failure model considers the influence of stress triaxiality, strain rate, and temperature on fracture strain [16]. The fracture strain is monotonically changed for the stress triaxiality. However, Bao and Wierzbicki [17, 18] found through many experiments that the fracture strain of

materials does not change monotonically concerning stress triaxiality. Moreover, a piecewise function expression was proposed, which is the B-W model. In 2010, Bai and Wierzbicki [19] introduced the stress triaxiality and Lode angle parameters based on the traditional Mohr-Coulomb criterion [20] and established the MMC model, which has better applicability and higher precision. The prediction parameters used in this model have also been modified for different materials. For example, Defaisse et al. [21] proposed a simple nonlinear damage accumulation rule based on the Rice and Tracey/Johnson Cook formulation with a Lode-dependent term for ultrahigh-strength steel. Ji et al. [22] and Tang et al. [23] used the MMC model to calibrate 6061-T5 aluminum alloy and Ti-6Al-4V titanium alloy and extended the application scope of the model to anisotropic materials. Based on the reasons for the formation of microscopic pores, Hu et al. [24] and Hung et al. [25] regarded the nucleation, growth, and aggregation of pores as functions related to normal stress or shear stress integrated into fracture track surfaces related to strain.

In 2016, Neukamm et al. [26–28] and Andrade et al. [29] developed and improved the damage model related to the generalized incremental stress state, the generalized incremental stress state dependent damage model, namely the generalized incremental stress state dependent damage model (GISSMO) failure model. The GISSMO failure model contains the fracture strain curve and the critical strain curve of the material. Damage accumulation is used as a criterion for evaluating material failure. In addition, the GISSMO failure model is an independent model that can be easily coupled with other material constitutive models. The fracture strain curve in the model can be obtained either by using the J-C model, the B-W model, and the MMC model or by performing finite element simulations with optimized parameters. Due to these characteristics, the GISSMO failure model can assess the fracture behavior of materials under multiple load paths. In recent years, some scholars have successfully predicted the fracture behavior of different metal materials using the GISSMO model. Zhang et al. [30] conducted tensile, and shear tests for 7075-T6 aluminum alloy and finally established the GISSMO model of the material considering the effect of grid size and verified the model's validity through a three-point bending test. Amer et al. [31] calibrated AA5754 aluminum alloy by Gurson, CDM, J-C, GISSMO, and other commonly used damage models, and verified by perforation test. The results showed that GISSMO model had the best prediction ability. Xiao et al. [32] established GISSMO failure model of 7003 aluminum alloy and used it to simulate a three-point bending test of an open-hole beam.

At present, in finite element simulations of collisions of key components of rail vehicles, the failure model of materials is mostly ignored [33]. The material studied in this paper is SUS301L-MT, which is mostly used for rail vehicle body structures, automobile bodies, and other structures [34]. Therefore, it is necessary to deeply analyze the fracture behavior of SUS301L-MT and improve the accuracy of the corresponding finite element simulations. The main contributions of this paper are as follows: (1) A quasi-static fracture experiment of SUS301L-MT under different stress states was carried out. The fracture strain of each specimen was obtained via DIC measurements. (2) Parameters of the GISSMO failure model for the material were calibrated with a wide range of stress triaxiality. (3) The GISSMO failure model of the SUS301L-MT was verified through simulations. (4) The limitations of the GISSMO failure model were discussed. The results can provide more accurate material parameters to improve the simulation accuracy to some extent.

2 Method and Experiment

2.1 Characteristics of the GISSMO Failure Model

The above studies show that the ductile fracture of metals is affected by the triaxiality of stress and the Lode angle. The stress triaxiality Eq. (1) is defined as follows:

$$\eta = \frac{\frac{1}{3}(\sigma_1+\sigma_2+\sigma_3)}{\sqrt{\frac{(\sigma_1-\sigma_2)^2+(\sigma_2-\sigma_3)^2+(\sigma_1-\sigma_3)^2}{2}}}, \tag{1}$$

where σ_1, σ_2, and σ_3 are the first, second and third principal stresses, respectively.

The relationship between the Lode angle parameter and the Lode angle is shown in Eq. (2) [35], For the plane stress state, Eq. (3) [35] is satisfied between the stress triaxiality and the Lode angle parameter, and Eq. (3) can be simplified accordingly to eliminate the influence of the Lode angle.

$$\overline{\theta} = 1 - \frac{6\theta}{\pi} = 1 - \frac{2}{\pi}\arccos\xi, \tag{2}$$

$$\xi = \cos(3\theta) = \cos\left[\frac{\pi}{2}\left(1-\overline{\theta}\right)\right] = -\frac{27}{2}\eta\left(\eta^2 - \frac{1}{3}\right), \tag{3}$$

where θ, $\overline{\theta}$, and ξ are Lode angle, normalized Lode angle and Lode angle parameter, respectively.

After continuing the advantages of the above fracture criterion model, the characteristics of the GISSMO failure model are described hereafter.

2.1.1 Damage Evolution [29]

For nonlinear strain path loading problems, the damage accumulation is also nonlinear. When the material is about

to fracture, the increment in the damage variable will be more significant, and the damage will accelerate.

The corresponding damage calculation Eq. (4) is as follows:

$$\Delta D = \frac{n}{\varepsilon_{\mathrm{f}}(\eta)} D^{(1-\frac{1}{n})} \Delta\varepsilon_{\mathrm{p}}, \tag{4}$$

where D is the damage variable, ΔD is the increment in the damage variable, $\Delta\varepsilon_{\mathrm{p}}$ is the increment in the plastic strain, and n is the nonlinear damage accumulation index. $\varepsilon_{\mathrm{f}}(\eta)$ is the plastic strain of the material, which is related to the stress triaxiality η.

2.1.2 Critical Plastic Strain and Stress/Damage Coupling [29]

There is a coupling relationship between damage accumulation and stress reduction. After the plastic strain reaches the critical strain, the flow stress gradually decreases due to damage accumulation. The calibration of whether stress decreases is a stability variable with a cumulative form similar to the damage variable. The equation for the stability variable is as follows:

$$\Delta F = \frac{n}{\varepsilon_{\mathrm{crit}}(\eta)} F^{(1-\frac{1}{n})} \Delta\varepsilon_{\mathrm{p}}, \tag{5}$$

where F is the stability variable, ΔF is the increment in the stability variable, and $\varepsilon_{\mathrm{crit}}(\eta)$ is the critical plastic strain of the material, which is related to the stress triaxiality η.

When F reaches 1, the stress begins to weaken. The weakened stress equation is as follows:

$$\tilde{\sigma} = \sigma_e[1 - \left(\frac{D_{\mathrm{d}} - D_{\mathrm{crit}}}{1 - D_{\mathrm{crit}}}\right)^m], \tag{6}$$

where D_{crit} is the damage variable when F accumulates to 1, m is the stress decrease index associated with damage, σ_e is the original stress, and $\tilde{\sigma}$ is the equivalent stress after attenuation.

The characteristics of the GISSMO failure model are described as follows. As the plastic strain increases, the stability variable F gradually increases. When F reaches 1, the stress begins to decrease due to damage. When D increases to 1, the material breaks, and the stress is reduced to 0 MPa.

The GISSMO failure model has been embedded in LS-DYNA and belongs to the "MAT_ADD_EROSION" model.

2.2 Experimental Material, Technique and Specimens

The composition of SUS301L-MT stainless steel in this paper is shown in Table 1, and the basic mechanical properties of this material are shown in Table 2.

Specimens are designed in the form of a sheet, which is taken from a stainless steel sheet with dimensions of 500 mm×500 mm×3 mm. The dimensions of the tensile testing specimens of several different stress states are shown in Figure 1. The thickness of these specimens is 1.5 mm. In reality, the stress state of the test specimen is triaxial from local necking to fracture. However, the thickness of test specimens is about 1.5 mm, and the minimum width is 5 mm. This ratio assures the validity of the plane stress state [29]. The DIC equipment measured the strain data in the test. In this paper, the pattern speckles were produced by cross-rolling, as shown in Figure 2a.

All experiments were carried out in the quasistatic condition and at room temperature by a quasistatic tensile testing machine. The extensometer was used to measure the displacement change of the 25 mm gauge section. A force sensor measured the change in tensile force during the tension process. The above two constitute the force-displacement curve of each test specimen. At the same time, the DIC strain test system acquires images under the light source during the test, as shown in Figure 2b. The theory is that the strain distribution can be calculated based on the position of speckles. The specific fracture position of each specimen was determined according to the acquired images. The Von-Mises equivalent strain was calculated by measuring the directional strain in the local area of the fracture location. Further, the change of the equivalent strain field on the surface of the specimen can be obtained, and the equivalent fracture strain can be measured. The loading speed of all specimens was set to 5 mm/min to avoid the effect of strain rate during the test.

Table 2 The basic mechanical properties of SUS301L-MT stainless steel

Elastic modulus (GPa)	Poisson's ratio	Yield stress (MPa)	Tensile strength (MPa)
208.5	0.33	578.3	1517.1

Table 1 Composition of SUS301L-MT stainless steel (mass fraction, %)

C	Si	Mn	P	S	Cr	Ni	N
≤0.030	≤1.000	≤2.000	≤0.045	≤0.030	16.000—18.000	6.000—8.000	≤0.200

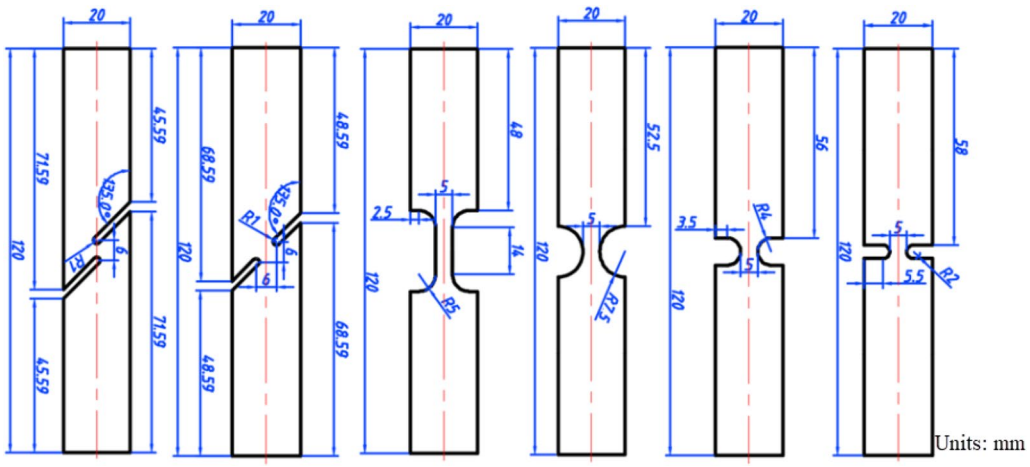

Figure 1 Specimens under different stress states

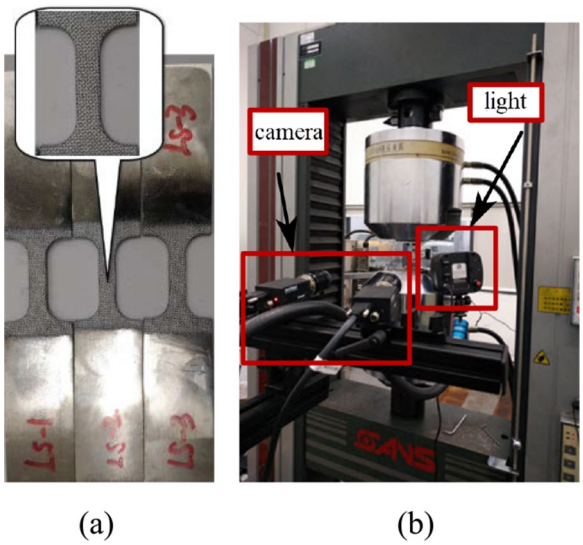

Figure 2 Specimens with speckle pattern and Quasi-static testing system

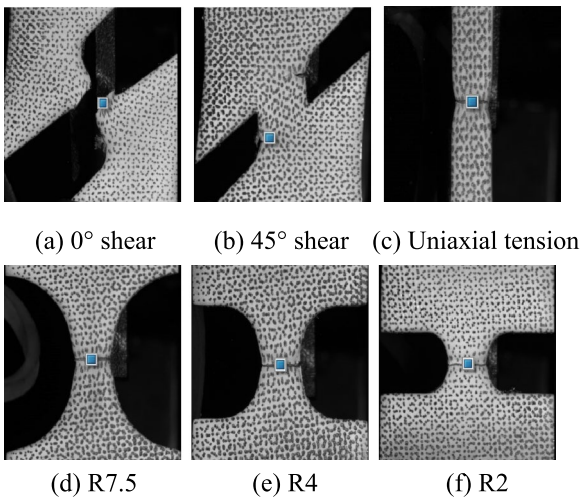

Figure 3 Fracture morphology and measured fracture strain under different stress states

2.3 Test Results

Tests under different stress states were carried out following the above test methods and the design specimens. The fracture behavior of the material under different stress states was obtained.

The fracture position of each specimen is determined according to the images obtained by the DIC equipment. 0° shear and 45° shear specimens cracked first at the minimum cross-section fillet position. Uniaxial and three kinds of notched specimens fractured in the middle of the minimum section. The fracture strain corresponding to different stress states was measured in the rectangular coverage area (as shown in Figure 3); the results are shown in Table 3.

Table 3 The fracture strain of specimens under different stress states

0° shear	45° shear	Uniaxial tension	Notched tension (R7.5)	Notched tension (R4)	Notched tension (R2)
1.39	1.21	1.28	0.99	0.86	0.68

The test results show that the fracture morphology is closely related to the stress state. The fracture strain of the material under different stress states is also different.

3 Calibration of the Model Parameters

According to the characteristics of the GISSMO failure model, the following parameters of SUS301L-MT are determined in this section:

(1) Relationship between the equivalent fracture strain and stress triaxiality.
(2) Relationship between the equivalent critical strain and stress triaxiality.
(3) Nonlinear damage accumulation index n_d.
(4) Stress reduction index m.

The stress triaxiality at each position is not constant but changes with time during material deformation. Considering the entire stress history can provide a more accurate prediction of ductile fracture. A finite element simulation is needed to estimate the stress triaxiality of each specimen with LS-DYNA software. The specimen models all use Belytschko-Tsay shell elements, and the mesh size is 0.5 mm. For the tensile testing specimens under different stress states, the fixed constraint and the constant velocity of the nodes are set as boundary conditions at the two ends of the specimen. The material model adopts MAT_PIECEWISE_LINEAR_PLASTICITY in software. The MTS testing machine carried out the uniaxial tensile test of the material, and the engineering stress-strain curve of the material was obtained by the DIC method. Due to the material's strong plasticity, the elastic deformation can be ignored, and the sample after the necking stress state is complex. The measurement result cannot reflect the accurate material mechanical properties. Therefore, the elastic section and necking section of the curve was removed, and the engineering stress-strain curve was transformed into a flow stress-real strain curve to reflect the natural mechanical properties of the material. The results are shown in Figure 4, and the curve was input into the finite element model. During the test, in order to avoid the influence of strain rate, the loading speed of all samples was 5 mm/min. However, the same loading speed used in the numerical analysis would have a significant time cost, so the speed of 1000 mm/s was adopted. Ref. [36] shows that when the kinetic energy accounted for the total energy ratio is small, the loading speed did not affect the results. The finite element models of the specimens under different stress states are shown in Figure 5. The stress triaxiality of each specimen are as shown in Table 4.

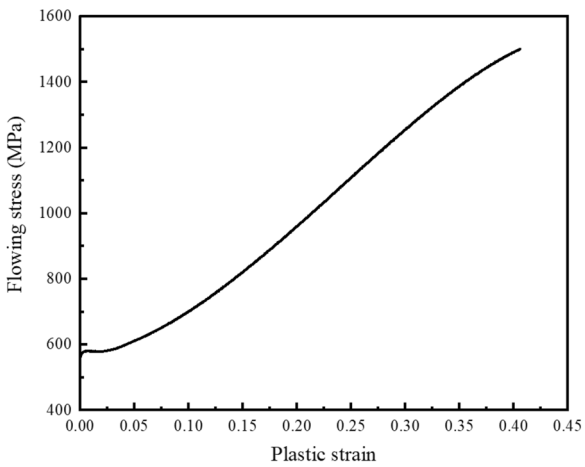

Figure 4 The hardening curve of SUS301L-MT

Except for the first parameter, the other parameters cannot be directly obtained from the test data. The optimization method in this paper mainly adopts LS-OPT optimization. For the GISSMO failure model, a set of certain n_d and m parameters must be applicable to all stress states. According to this characteristic, the idea of parameters optimization is as follows. First, the parameters n_d and m are defined by the LS-OPT optimization method. Then, the relationship between the critical strain and stress triaxiality is refined according to the test results.

The n_d and m of simple stress states, including uniaxial tension and notched tension, are preferentially determined. Based on this information, the critical strain values under different stress states are defined for these three specimen types. Then, the parameters of

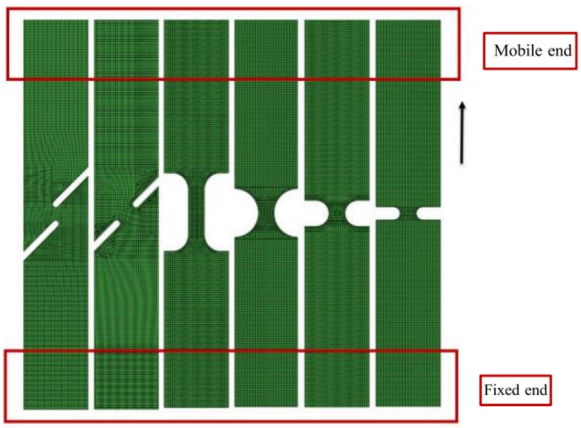

Figure 5 Finite element models of specimens

Table 4 Average stress triaxiality of specimens under different stress states

0° shear	45° shear	Uniaxial tension	Notched tension (R7.5)	Notched tension (R4)	Notched tension (R2)
0.113	0.373	0.333	0.389	0.451	0.498

the remaining complex stress states are finally obtained by local corrections. The overall optimization process is shown in Figure 6. Figure 7 shows the LS-OPT optimization process for the uniaxial tension specimen. Firstly, select the finite element model to be calculated and complete the solver setting. n_d, m, and critical strain are defined as variables and given initial values. The optimization interval was set, the target curve was set as the force-displacement curve measured in the test, the calculation curve was the force-displacement curve calculated by the finite element method, and the optimization algorithm and cut-off standard were set. Finally, the suitable parameters n_d, m, and critical strain values of the model are found through several automatic iterative calculations. The other tensile testing specimens were sequentially optimized according to the same procedure. After several calculations, $n_d = 0.68$, and $m = 1.05$.

Eventually, the fracture strain and critical strain for seven stress states, the 0° shear, the uniaxial tension, notched tension (R2, R4, R7.5), and biaxial tension, are obtained. Then, the fracture strain curve and critical strain curve after spline interpolation are shown in Figure 8.

It can be seen from Figure 8 that within the range of stress triaxiality of 0.1−0.5, the critical strain is less than the fracture strain. The closer the triaxiality value is to 0.333, the more significant the difference between the two, and the more pronounced the softening behavior of the material is, which is consistent with the necking degree near the fracture of different specimens shown in Figure 3. When stress triaxiality is less than 0.1 and greater than 0.5, the critical strain is greater than the fracture strain. That is, the fracture occurs directly without softening behavior. This phenomenon is because the micropores' shape is more likely to change than the volume of the material when it is sheared. The pores are elongated and connected along the shear direction to form cracks, which can be regarded as the transient fracture of the material. When the material is subjected to biaxial tensile stress, no necking occurs, which can be regarded as no softening behavior.

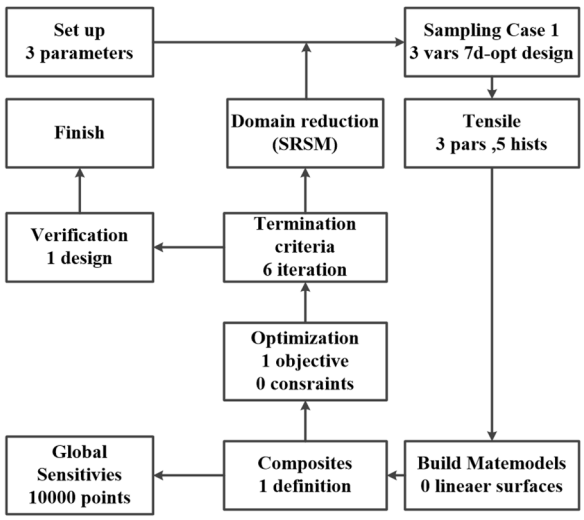

Figure 7 LS-OPT optimization process for the uniaxial tension specimen

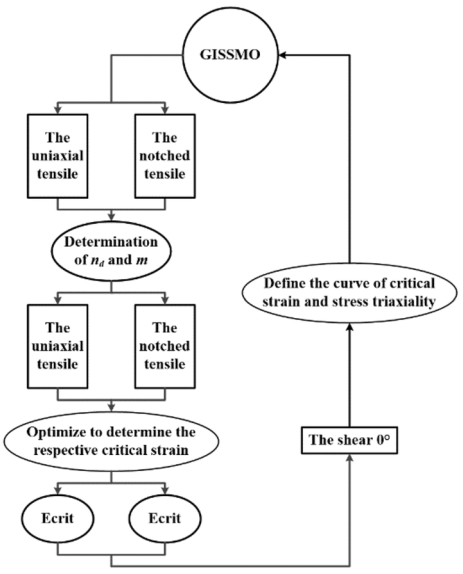

Figure 6 Overall optimization flowchart

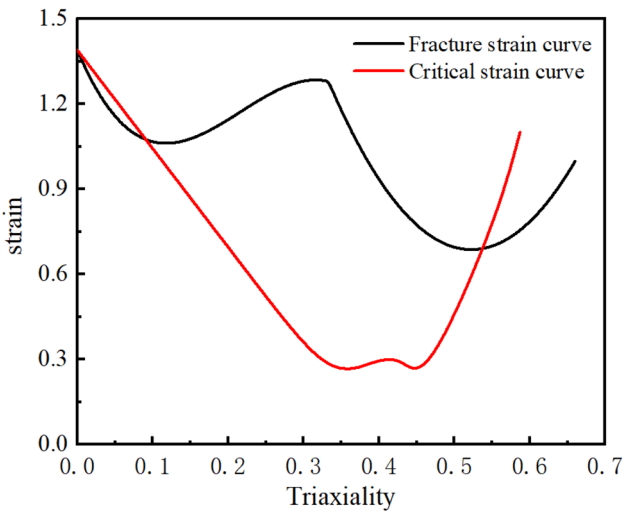

Figure 8 Equivalent fracture strain curve and equivalent critical strain curve after interpolation

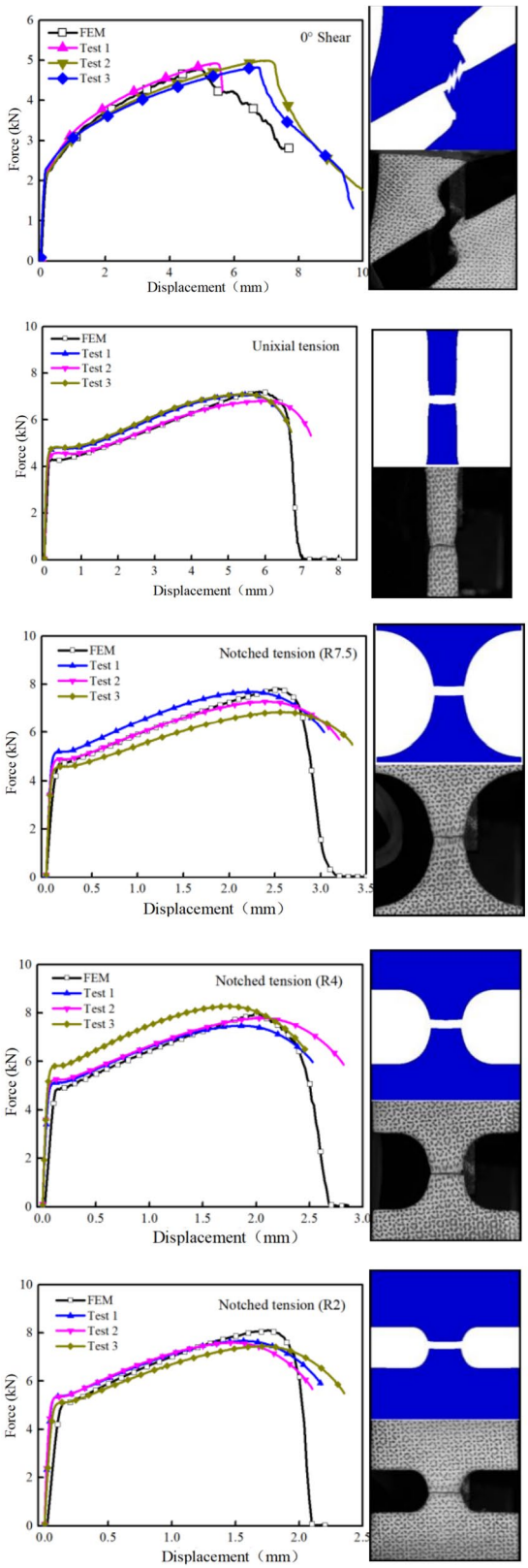

(a) Force-displacement curve (b) Fracture morphology

Figure 9 Comparison of test and simulation of perforated specimens

4 Discussions and Verification

After the optimization process described above, the parameters of the GISSMO failure model suitable for SUS301L-MT were obtained. The simulation results are compared with the test results, as shown in Figure 9. The mean square deviation evaluates the error between the simulation and the test. The mean square deviation is calculated according to Eq. (7), and the results are shown in Table 5.

$$\varepsilon_{\text{error}} = \frac{1}{P}\sum_{P=1}^{P} W_P \left(\frac{f_p - G_P}{s_p}\right)^2 = \frac{1}{P}\sum_{P=1}^{P} W_P \left(\frac{e_p}{s_p}\right)^2, \tag{7}$$

where P is the number of statistical analysis points, f is the calculated data points, G is the target data points, S is the maximum value in the target data points, and W is the weight; W=1.

The fracture position and force-displacement curves of the simulation results based on the GISSMO failure model of SUS301L-MT in this paper agree with the experimental results under different stress states. The notched tension (R4) specimen has the slightest mean square deviation (0.95%) between the simulated and experimental force-displacement curves. In contrast, the notched tension (R2) specimen has the most significant mean square deviation (4.67%) between the simulated and experimental force-displacement curves. In general, the simulation results based on the GISSMO failure model agree well with the experimental results in both the force-displacement curve and the fracture morphology.

The 45° shear specimen was not considered during the establishment of the GISSMO failure model. The stress triaxiality in the 45° shear stress state is between that in the 0° shear and perforation stress states. In order to ensure the accuracy of the failure model obtained in this paper, a 45° shear specimen composed of SUS301L-MT was simulated, and the simulation results were compared with the experimental results. The results of the force-displacement curve and the fracture morphology are shown in Figure 10. The crack initiation position and the fracture morphology in the simulation are consistent with the experimental results. For the force-displacement curve, the overall trend of the test curve and the simulation curve is basically similar, and the mean square deviation between the two curves is 3.01%. Furthermore, the error in fracture displacement between the simulation and experiment is relatively tiny.

Table 5 Mean square deviation of simulation and test results for the force-displacement curves under different stress states (%)

0° shear	Uniaxial tension	Notched tension (R7.5)	Notched tension (R4)	Notched tension (R2)
2.27	2.48	4.5	0.95	4.67

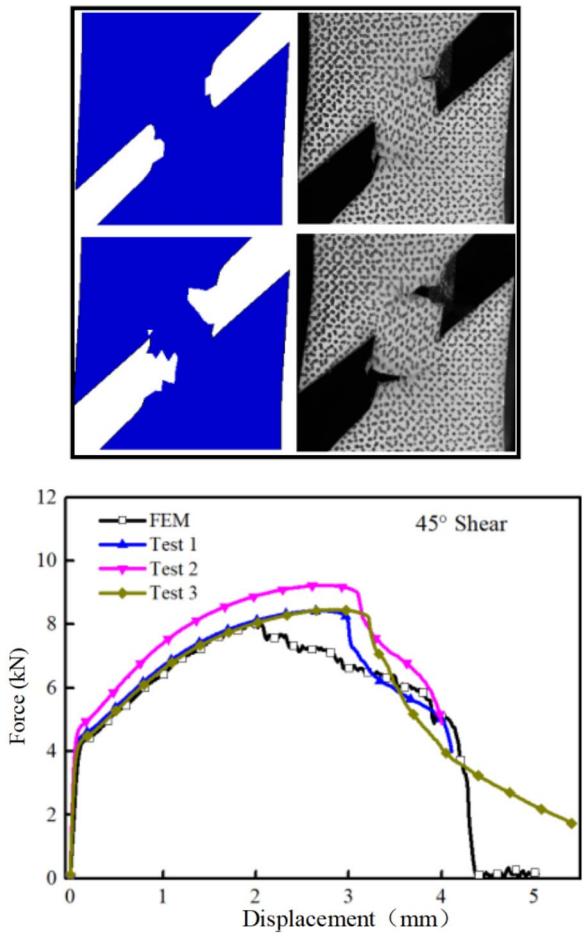

Figure 10 Comparison of simulated and experimental fracture morphology of the 45° shear specimen

5 Mesh Dependency

In the above studies, the calibrated GISSMO model parameters are only suitable for mesh sizes around 0.5 mm. For deformations with strain localization, the mesh size significantly affects the simulation results. This phenomenon is most evident in uniaxial tension for several fracture tests carried out in this paper. Therefore, taking uniaxial tension as an example, four different mesh sizes (0.5 mm, 1 mm, 2.5 mm, 5 mm) as shown in Figure 11 are adopted, and their numerical results are compared.

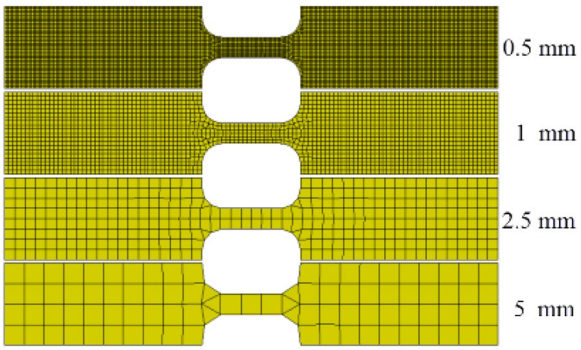

Figure 11 Finite element models of different mesh sizes

The strain distribution and the force-displacement curve at the moment before fracture obtained from the simulation calculation of different element sizes are shown in Figure 12, respectively. The results show that the strain distribution at the moment before fracture is quite different for different mesh sizes. When the element size is small, the local necking of the specimen is obvious. As the mesh size increases, the difference from the test phenomenon becomes larger.

In order to address this problem, there is a correction function for the fracture strain in the GISSMO failure model. The damage variable is modified during the damage accumulation process, which accelerates the damage accumulation at large sizes, as shown in Eqs. (8)−(10) [35]:

$$\Lambda(L_e,\eta)=\begin{cases}\beta_{\text{shear}}, & \eta\le 0,\\ \left\{\frac{\alpha(L_e)-\beta_{\text{shear}}}{1/3}\right\}\eta+\beta_{\text{shear}}, & 0<\eta\le 1/3,\\ \left\{\frac{\alpha(L_e)-\beta_{\text{biaxial}}}{1/3}\right\}\eta+\beta_{\text{biaxial}}, & 1/3\eta<2/3,\\ \beta_{\text{biaxial}}, & \eta\ge 2/3,\end{cases} \tag{8}$$

$$\beta_{\text{shear}}=1-[1-\alpha(L_e)](1-k_{\text{shear}}), \tag{9}$$

$$\beta_{\text{biaxial}}=1-[1-\alpha(L_e)](1-k_{\text{biaxial}}), \tag{10}$$

where $\alpha(L_e)$ is a function of the fracture strain correction factor and the element size in a uniaxial tensile test; β_{shear}, β_{biaxial}, k_{shear} and k_{biaxial} are correction functions and reduction factors under pure shear and biaxial stress states, respectively.

In the LS-DYNA software, the uniaxial tensile test is used as a reference to determine the strain correction factor at different mesh sizes, as shown in Figure 13.

The corrected force-displacement curve results are shown in Figure 14. The results show that after correction, the macroscopic numerical results of different mesh sizes are basically consistent with the experimental results.

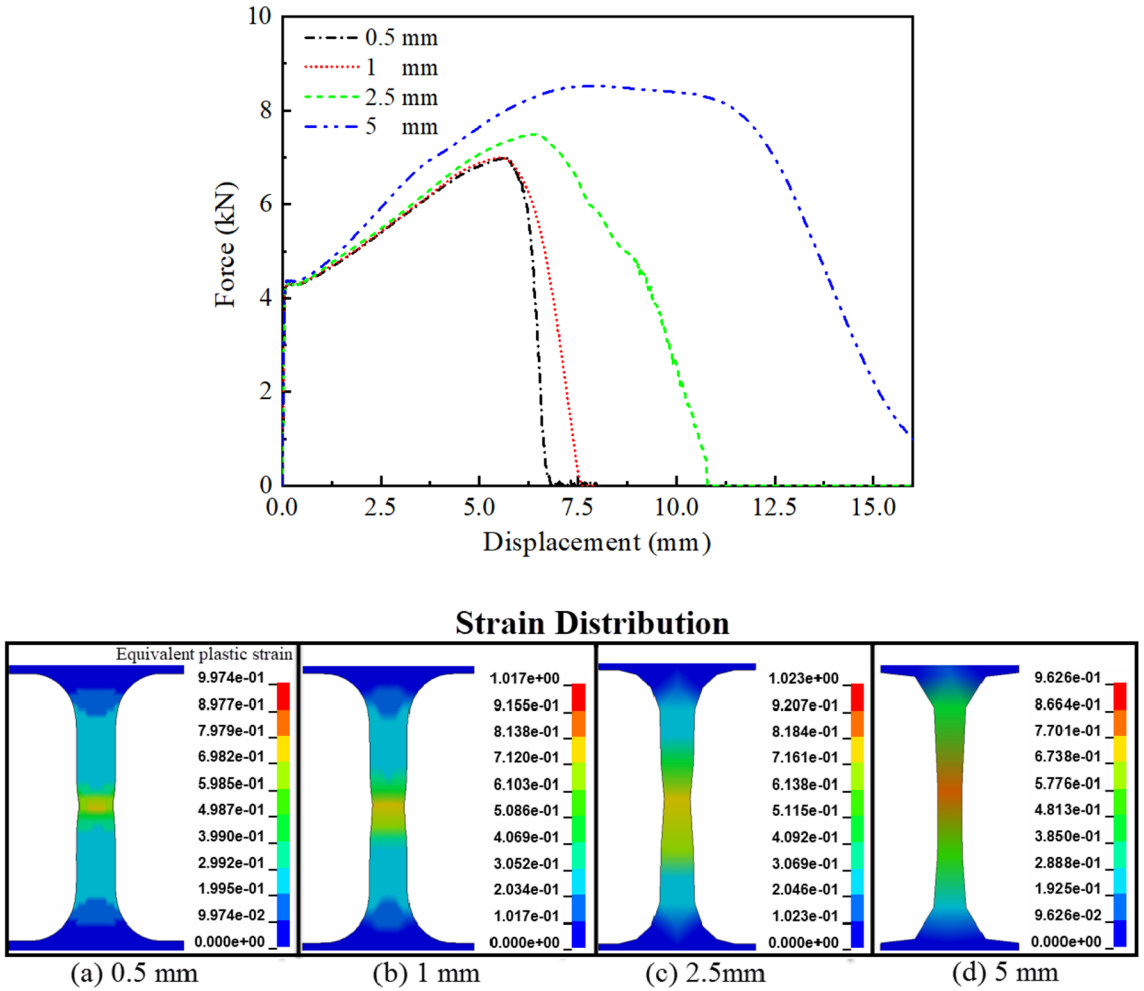

Figure 12 Force-displacement curves and equivalent strain distributions for different mesh sizes

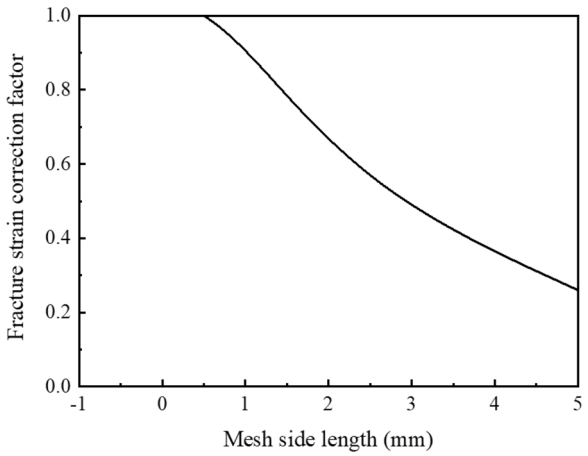

Figure 13 Correction factor curve for mesh size

However, the strain distribution under different element sizes after correction is shown in Figure 14. It can be seen from the figure that despite the mesh size correction, the deviation is still significant for the strain distribution before fracture. In summary, numerical results with inappropriate mesh sizes can cause large deviations. Therefore, for large-scale structural simulation, the GISSMO failure model may result in an excessive calculation, which is a major drawback of the GISSMO failure model at present.

6 Conclusions

To investigate the fracture behavior of SUS301L-MT, fracture tests were carried out under different stress states. The fracture strain data under different stress states were obtained from the test results. Parameters of the GISSMO failure model were calibrated for

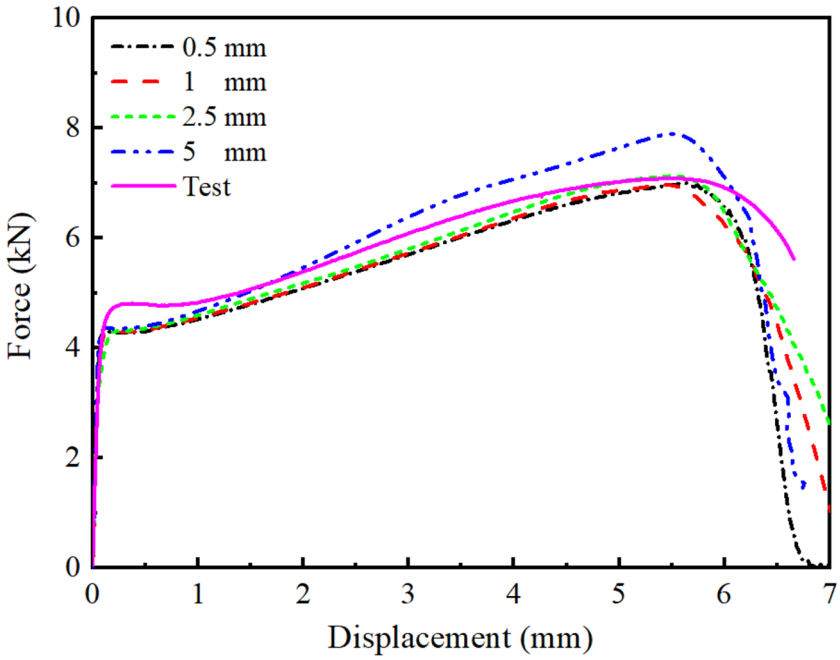

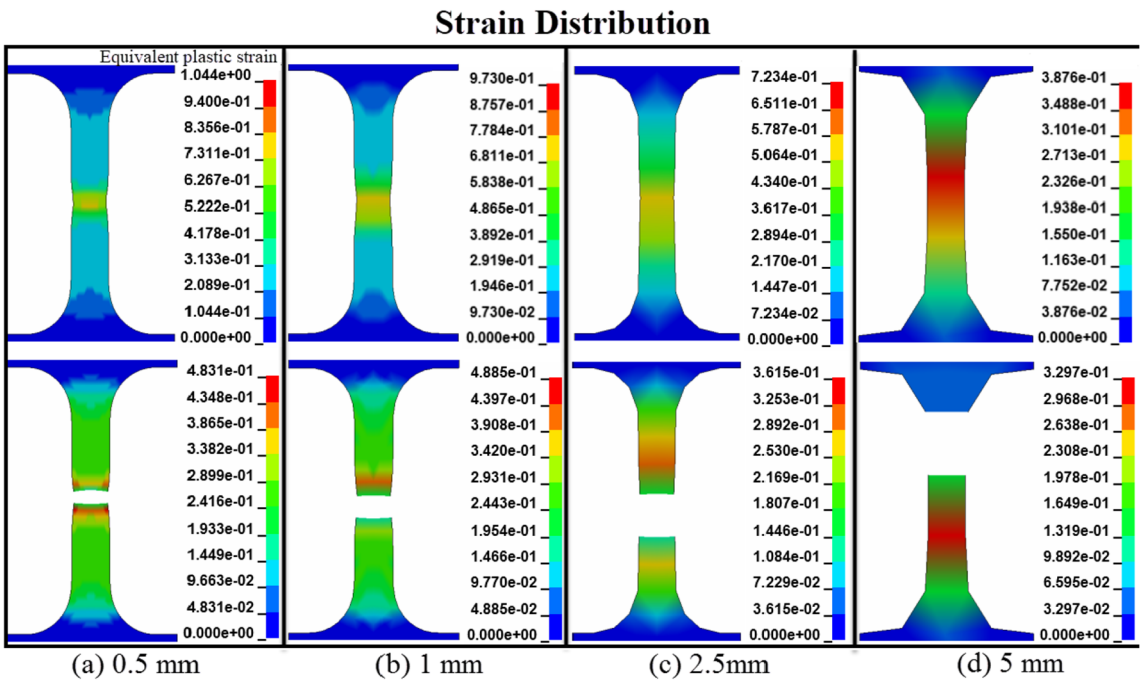

Figure 14 Force-displacement curve and equivalent strain distribution after size correction

SUS301L-MT, and the model's accuracy was verified. Finally, the mesh dependency of this model was discussed. The main conclusions were as follows:

(1) The fracture strain curve and critical strain curve of SUS301L-MT were obtained by quasi-static fracture test and parameter calibration, respectively, and the difference between them increased first and then decreased with the increase of stress triaxiality. This phenomenon is due to the rapid deformation and coalescence of the holes under shear stress and the absence of necking under biaxial tensile stress.
(2) Based on the calibrated GISSMO failure model of SUS301L-MT, finite element simulations of dif-

ferent specimens were carried out. The fracture morphology and force-displacement curves from the simulation were agreed with the experimental results. The minimum mean square deviation between each sample's simulated and experimental force-displacement curves is 0.95%, and the maximum is 4.67%. The simulation results were consistent with the test results regarding the force-displacement curve and fracture mode.

(3) The GISSMO failure model was verified with test results from a 45° shear specimen. The crack initiation position and subsequent fracture behavior in the simulation were consistent with the experimental results. The mean square error between the simulation and the test was 3.01% for the force-displacement curve. Moreover, the error in fracture displacement between the simulation and experiment was relatively small. Thus, the GISSMO failure model accurately reflected the fracture failure characteristics of the material.

However, the mesh dependency has not been completely resolved. Although the error of the force-displacement curve is reduced, the large mesh will still lead to a large deviation of strain distribution. It has a certain influence on the numerical calculation of large-scale mechanical structures.

Acknowledgements
Not applicable.

Authors' Contributions
TZ was in charge of the whole trial; HD wrote the manuscript; YL assisted with sampling and laboratory analyses. All authors read and approved the final manuscript.

Authors' Information
Tao Zhu, born in 1984, is currently an associate professor at *Southwest Jiaotong University, China*. He received his bachelor degree from *Southwest Jiaotong University, China*, in 2012. His research interests include rolling stock strength and train crash dynamics. Tel: +86-28-87634909
Haoxu Ding, born in 1998, is currently a master candidate at *State Key Laboratory of Traction Power, Southwest Jiaotong University, China*.
Chao Wang, born in 1995, is currently a PhD candidate at *State Key Laboratory of Traction Power, Southwest Jiaotong University, China*.
Yuxin Liu, born in 1994, is currently a r&d designer at *FAW Jiefang Automobile Co., LTD*. He received his master's degree from *State Key Laboratory of Traction Power, Southwest Jiaotong University*, in 2021. His research interests include dynamic mechanical properties and fracture of materials.
Shoune Xiao, born in 1964, is currently a professor at *Southwest Jiaotong University, China*. His research interests include rolling stock strength and train crash dynamics.
Guangwu Yang, born in 1977, is currently a professor at *Southwest Jiaotong University, China.* His main research interests include vibration fatigue of rolling stock structure.
Bing Yang, born in 1979, is currently a professor at *Southwest Jiaotong University, China.* His main research interests include material fatigue and fracture.

Funding
Supported by National Natural Science Foundation Project of China (Grant No. 52172409) and Sichuan Provincial Outstanding Youth Fund of China (Grant No. 2022JDJQ0025).

Availability of data and materials
The datasets supporting the conclusions of this article are included within the article.

Competing Interests
The authors declare no competing financial interests.

Received: 10 June 2021 Revised: 4 January 2023 Accepted: 6 January 2023
Published online: 15 February 2023

References

[1] C N Yan, Z N Li. Studies on simulation of metal ductile fracture process with application of damage criterion. *Journal of Mechanical Strength*, 2001, 33(5): 754–758.
[2] R Liu, X J Wang, P W Chen, et al. The role of tension-compression asymmetrical microcrack evolution in the ignition of polymer-bonded explosives under low-velocity impact. *Journal of Applied Physics*, 2021, 129(17): 175108.
[3] A S Bouchikhi. Numerical investigation of fracture in double-edge notched FGM plates under tension load. *International Journal of Structural Integrity*, 2019, 10(6): 838–849.
[4] R Daud, W Xu, I Ibrahim, et al. Effect of chewing and cutting condition for V-shape three-dimensional titanium miniplate for fixation of mandibular angle fractures (MAFs). *International Journal of Structural Integrity*, 2020, 11(4): 625–631.
[5] M H Yu. Advances in strength theories for materials under complex stress state in the 20th Century. *American Society of Mechanical Engineers*, 2002, 5(3): 169–218.
[6] F A McClintock. A criterion for ductile fracture by the growth of holes. *Journal of Applied Mechanics*, 1968, 35(2): 363–371.
[7] A L Gurson. Continuum theory of ductile rupture by void nucleation and growth: Part I—yield criteria and flow rules for porous ductile media. *Journal of Engineering Materials & Technology*, 1977, 99(1): 297–300.
[8] J R Rice, D M Tracey. On the ductile enlargement of voids in triaxial stress fields. *Journal of the Mechanics & Physics of Solids*, 1969, 17(3): 201–217.
[9] V Tvergaard. Influence of voids on shear band instabilities under plane strain conditions. *International Journal of Fracture*, 1981, 17(4): 389–407.
[10] V Tvergaard. On localization in ductile materials containing spherical voids. *International Journal of Fracture*, 1982, 18(4): 237–252.
[11] V Tvergaard, A Needleman. Analysis of the cup-cone fracture in a round tensile bar. *Acta Metallurgica*, 1984, 32(1): 157–169.
[12] A Needleman, V Tvergaard. An analysis of ductile rupture in notched bars. *Journal of the Mechanics and Physics of Solids*, 1984, 32(6): 461–490.
[13] A Ramazani, M Abbasi, U Prahl, et al. Failure analysis of DP600 steel during the cross-die test. *Computational Materials Science*, 2012, 64: 101–105.
[14] Z X Li. *Damage mechanics with application*. Beijing: Science Press, 2002. (in Chinese)
[15] C Z Li, X Q Chang, Y P Zheng. The simulation of crack growth in viscous elastic materials. *Journal of Mechanical Strength*, 2007, 28(5): 827–830. (in Chinese)
[16] G R Johnson, W H Cook. Fracture characteristics of three metals subjected to various strains, strain rates, temperatures and pressures. *Engineering Fracture Mechanics*, 1985, 21(1): 31–48.
[17] Y Bao, T Wierzbicki. On fracture locus in the equivalent strain and stress triaxiality space. *International Journal of Mechanical Sciences*, 2004, 46(1): 81–98.
[18] T Wierzbicki, Y Bao, Y W Lee, et al. Calibration and evaluation of seven fracture models. *International Journal of Mechanical Sciences*, 2005, 47(4): 719–743.
[19] Y Bai, T Wierzbicki. Application of extended Mohr–Coulomb criterion to ductile fracture. *International Journal of Fracture*, 2010, 161: 1–20.
[20] M Dunand, D Mohr. On the predictive capabilities of the shear modified Gurson and the modified Mohr–Coulomb fracture models over a wide range of stress triaxialities and Lode angles. *Journal of the Mechanics & Physics of Solids*, 2011, 59(7): 1374–1394.

[21] C Defaisse, M Mazière, L Marcin, et al. Ductile fracture of an ultra-high strength steel under low to moderate stress triaxiality. *Engineering Fracture Mechanics*, 2018, 194: 301–308.
[22] C Ji, Z G Li, J G Liu. Development of an improved MMC-based fracture criterion characterizing the anisotropic and strain rate-dependent behavior of 6061-T5 aluminum alloy. *Mechanics of Materials*, 2020, 150: 103598.
[23] B T Tang, Q F Wang, N Guo, et al. Modeling anisotropic ductile fracture behavior of Ti-6Al-4V titanium alloy for sheet forming applications at room temperature. *International Journal of Solids and Structures*, 2020, 207(1): 178–195.
[24] Q Hu, X F Li, X H Han, et al. A new shear and tension based ductile fracture criterion: Modeling and validation. *European Journal of Mechanics - A/Solids*, 2017, 66: 370–386.
[25] Q Hung, J J Kim, D T Nguyen, et al. Uncoupled ductile fracture criterion considering secondary void band behaviors for failure prediction in sheet metal forming. *International Journal of Mechanical Sciences*, 2020, 169: 105297.
[26] F Neukamm, M Feucht, Roll K, et al. On closing the constitutive gap between forming and crash simulation. *Proceedings of International Ls-Dyna® Users Conference*, 2008.
[27] F Neukamm, M Feucht, A Haufe. Considering damage history in crashworthiness simulations. *Proceedings of European Ls-dyna Conference*, 2009.
[28] M Feucht , F Neukamm, A Haufe. A phenomenological damage model to predict material failure in crashworthiness applications. *Recent Developments and Innovative Applications in Computational Mechanics*, Springer, Berlin, Heidelberg, 2011: 143–153.
[29] F X C Andrade, M Feucht, A Haufe, et al. An incremental stress state dependent damage model for ductile failure prediction. *International Journal of Fracture*, 2016, 200(1–2): 1–24.
[30] Z Q Zhang, Y J Cui, G Yu. Damaged and failure characterization of 7075-T6 Al alloy based on GISSMO model. *Journal of Mechanical Science and Technology*, 2021, 3: 1209–1214.
[31] M Amer, M Shazly, M Mohamed, et al. Ductile damage prediction of AA 5754 sheet during cold forming condition. *Journal of Mechanical Science and Technology*, 2020, 34(10): 4219–4228.
[32] Y Xiao, Y M Hu. Numerical and experimental fracture study for 7003 aluminum alloy at different triaxialities. *Metals and Materials International*, 2020, 1900: 1–13.
[33] Y Feng, S N Xiao, T Zhu, et al. Influence of material strain rate effect on crashworthiness of two kinds of e nergy-absorbing structure. *Journal of Central South University (Science and Technology)*, 2018, 49(10): 2625–2635. (in Chinese)
[34] J X Huang. A new application field of stainless steel in china—urban railway vehicles. *China Metallurgy*, 2005, 15(10): 4–6. (in Chinese)
[35] Y Bai, T Wierzbicki. A new model of metal plasticity and fracturewith pressure and Lode dependence. *International Journal of Plasticity*, 2008, 24(6): 1071–1096.
[36] G Gruben, O S Hopperstad, T Børvik. Evaluation of uncoupled ductile fracture criteria for the dual-phase steel Docol 600DL. *International Journal of Mechanical Sciences*, 2012, 62: 133–146.